Marine and Petroleum Geology 112 (2020) 104058

Contents lists available at ScienceDirect

Marine and Petroleum Geology

journal homepage: www.elsevier.com/locate/marpetgeo

Research paper

Pore structural evolution of shale following thermochemical treatment

Sean P. Rigby[a,b,*], Hosne Jahan[a,b], Lee Stevens[a], Clement Uguna[a], Colin Snape[a], Bill Macnaughton[c], David J. Large[a], Robin S. Fletcher[d]

[a] Department of Chemical and Environmental Engineering, University of Nottingham, University Park, Nottingham, NG7 2RD, United Kingdom
[b] Geo-energy Research Centre, University of Nottingham, University Park, Nottingham, NG7 2RD, United Kingdom
[c] Food Sciences, University of Nottingham, Sutton Bonington Campus, Sutton Bonington, Leicestershire, LE12 5RD, United Kingdom
[d] Johnson Matthey, P.O. Box 1, Belasis Avenue, Billingham, Cleveland, TS23 1LB, United Kingdom

ARTICLE INFO

Keywords:
Shale
Pyrolysis
In-situ combustion
Pore network
Gas sorption
Mercury porosimetry
X-ray tomography

ABSTRACT

Shales experience heat treatment concurrent with the presence of water or steam during reservoir engineering interventions, such as high pressure water fracking and in-situ combustion of hydrocarbons. This work utilises a novel technique, which is a combination of gas sorption overcondensation and integrated mercury porosimetry experiments, not used before for any type of porous material, to study the pore structure of a shale rock, and its evolution following thermal treatment in the presence of water. Overcondensation allows the extension of gas sorption beyond the limits of conventional experiments to enable direct study of macroporosity. Scanning curve experiments, initiated from the complete boundary desorption isotherm, that can only be obtained for macropores by overcondensation experiments, has revealed details of the relative pore size spatial disposition within the network. In particular, it has been found that the new large voids formed by treatment are shielded by relatively much narrower pore windows. Use of a range of different adsorbates, with differing polarity, has allowed the chemical nature of the pore surface before and after treatment to be probed. Integrated rate of gas sorption and mercury porosimetry experiments have determined the level of the particular contribution to mass transport rates of the newly introduced porosity generated by thermal treatment. Combined CXT and mercury porosimetry have allowed the mapping of the macroscopic spatial distribution of even the new mesoporosity, and revealed the degree of pervasiveness of the new voids that leads to a thousand-fold increase in mass transport on thermal treatment.

1. Introduction

Shale rocks can be either reservoirs for oil and gas, themselves, or cap-rocks and inter-layers in other types of reservoir. Such shales potentially undergo simultaneous treatment with heat and water as the result of reservoir engineering interventions, such as high pressure water fracking, and in-situ combustion of hydrocarbons (Lore et al., 2002). Thermal treatment in the presence of water can lead to internal structural modification of the pore structure of the shale. This structural modification would affect the hydrocarbon storage capacity and mass transport properties of the rock, thereby impacting such things as the seal integrity of cap-rocks. It is thus necessary to understand the likely changes that occur in the pore structure-transport relationships of shales as a result of treatment.

In the case of in-situ combustion processes for production of heavy oil an increase in the permeability of the shale cap-rock of a bitumen deposit could potentially lead to a critical incident. The partial combustion of the heavy oil is used to generate heat and steam to mobilise the rest of the oil. Ahead of the advancing flame front, additional fronts of combustion gases and steam at high pressure and temperature are also generated, reaching up to ~600–900 °C at the top of the tar sand seam (Greaves et al., 2012). These temperatures are high enough to achieve metamorphisation of mud-rocks and shales. The pace of the progression of these successive fronts is roughly 12–24 cm day^{-1} and the thickness of the combustion zone is ~20–30 m, and thus the cap-rocks are thermally treated in the presence of water for some time during the process. Further, in-situ combustion processes sometimes include periods of additional water or steam injection (known as 'wet combustion'), interspersed in periods of air injection, which lead to cyclic cooling of the reservoir.

The cap-rock for one reservoir rock can form some, or all, of the basement for another reservoir rock. For example, a small sandstone gas

* Corresponding author. Department of Chemical and Environmental Engineering, University of Nottingham, University Park, Nottingham NG7 2RD, United Kingdom.
E-mail address: enzspr@exmail.nottingham.ac.uk (S.P. Rigby).

https://doi.org/10.1016/j.marpetgeo.2019.104058
Received 8 April 2019; Received in revised form 19 September 2019; Accepted 23 September 2019
Available online 26 September 2019

reservoir occurs above the cap-rock for tar sands deposits in the McMurray Formation (Petrobank, 2008, 2010). Pooladi-Darvish and Mattar (2002) reported similar observations in another project site in the Athabasca region. Hence, before an in-situ combustion recovery technique could be safely employed, the effectiveness of a cap-rock, in providing the necessary sealing, separating say the tar sand and gas, would need to be investigated. This would involve establishing whether a direct hydraulic communication between the tar sand reservoir, and the overlaying gas deposit would occur due to the severe thermal and chemical (thermochemical) treatment conditions that the in-situ combustion process imposes on the cap-rock. This consideration is critical for the deployment of the Toe-to-Heel Air Injection (THAI) in-situ combustion process, where maintaining the stability of the combustion front is key to the success of achieving continuous oil production (Greaves et al., 2012). Hence, the injected air, to support the combustion, must be restricted to the tar sand reservoir for two reasons: (i) the continuity of the process, so that enough air always reaches the combustion front to maintain economical air-to-oil ratio, and (ii) the prevention of auto-ignition of the overlying gas in the event where enough heat, from the bitumen combustion zone, is conducted, or convected, or both, to the gas reservoir. Field scale simulations have been conducted to determine the impact of a permeable cap-rock on the THAI process (Rabiu Ado, 2017; Rabiu Ado et al., 2019). However, it is necessary to determine the impact of the thermochemical treatment on actual shale rocks to provide parameters for the reservoir simulations, such as the likely order of changes to mass transport rates on thermochemical treatment. It is the purpose of this work to assess the pore structure, and mass transport property, changes in a typical shale rock.

Shale is typically a poorly defined term that encapsulates a wide mixture of lithotypes and lithofacies. Further, a given shale is typically a highly heterogeneous material, and porosity can exist, or be introduced, over a wide range of length-scales, from nanometres to hundreds of micrometres. Typically, there is only one technique whereby all of this wide pore size range can be probed within the same experiment, namely mercury porosimetry. However, conventional mercury porosimetry suffers from several drawbacks. Mercury porosimetry is an indirect method and a model pore network structure is required to incorporate spatial pore size heterogeneity into interpretation of porosimetry data alone (Matthews and Spearing, 1992: Matthews et al., 1995; Tsakiroglou and Payatakes, 1991).

While mercury porosimetry can provide data for a substantial sample volume that can exceed the correlation length of the void space, the sample volume that can be realistically studied with more direct, imaging techniques is generally very much smaller, and, often, not statistically representative. This is because to directly image the void space at nanometre resolution with electron tomography or computerised X-ray tomography (CXT), even with a synchrotron, requires that sample sizes do not exceed the ~100 s nm to microns scale. Lin et al. (2016) did probe the macroscopic variation in sub-CXT-resolution porosity by impregnating the void space with high X-ray contrast salt solution, but this technique did not provide any information on the spatial variation of microscopic pore sizes. However, the lack of direct spatial information on pore size disposition from conventional mercury porosimetry, and the limitations on the sample volume for which nano-scale information can be directly obtained with conventional imaging, can be overcome by the combination of mercury porosimetry with CXT to image the macroscopic spatial variation of even nano-scale pore sizes (Nepryahin et al., 2016). Previously, Wood's metal injection has been combined with imaging via electron microscopy to obtain similar information for shales (Klaver et al., 2015). However, the combined Wood's metal intrusion and SEM method often has lower ultimate intrusion pressures than mercury porosimetry (and thus probes a narrower range of pore sizes), is prone to artefacts introduced in the sample polishing procedure, and the imaging is only for 2D sections, rather than the full 3D reconstructions available from CXT. CXT has been used to study thermally-induced pore structure changes in shales but was limited to mapping overall accessible porosity variation (Glatz et al., 2016). Combined mercury porosimetry and CXT have been used to study accessible porosity in rocks (Klobes et al., 1997; Fusi and Martinez-Martinez, 2013). However, in this work, mercury porosimetry and CXT experiments will also be serially integrated with gas sorption isotherms obtained both before and after entrapment. Hence, both macroscopic and nanoscopic information on the location and spatial arrangement of mercury entrapped following intrusion down to particular pore neck sizes can be obtained.

In addition, in this study, the working pore size range that can be probed by nitrogen sorption will be extended well into the macropore region, to largely match the potential capabilities of mercury porosimetry, using the overcondensation technique (Aukett and Jessop, 1996). Overcondensation can detect pores that are too large to achieve condensation within during conventional adsorption experiments, but that are also shielded by pores too small to be intruded during mercury porosimetry. The gas overcondensation technique will also be combined with scanning loop experiments, since these can be used to determine more information on the pore network structure (Liu et al., 1993; Esparza et al., 2004). These experiments will be used to reveal details of the morphology of the pore network introduced by thermochemical treatment. Further, the novel integrated rate of gas adsorption and mercury porosimetry technique (Nepryahin et al., 2016) will be used to determine the particular importance to mass transport of specific sub-sets of the shale pore network by removing them with entrapped mercury. This will be applied to determine the particular impact of the new pores generated by thermochemical treatment to mass transport.

2. Materials and methods

2.1. Samples studied

An Upper Bowland Shale sample was used in a case study of the behaviour of a shale rock during hydrothermal treatment. The shale sample were obtained from the Rempstone-1 well on the southern edge of the Widmerpool Gulf basin in the East Midlands of the U.K. The shale rock investigated is from a borehole of Arnsbergian age strata obtained at a depth of between 665 and 667 m. The Carboniferous, basal Namurian, Upper Bowland Shale Formation was deposited in parts of the East Midlands, North Wales and Northern England in a series of subsiding grabens and half-grabens (Fraser and Gawthorpe, 1990; Leeder, 1982, 1988). The Formation consists of marine, hemipelagic shales deposited in the basins. In the Widmerpool Trough, which is the location of the Remsptone-1 well in the East Midlands, the Bowland Shale is underlain by the Widmerpool Formation and other Visean shales. Cessation of rifting occurred across large parts of the UK during the late Visean and was followed by a period of regional thermal subsidence. Shale deposition continued in the Widmerpool Trough, culminating with the siliclastic sandstones of the Millstone Grit Group. These sandstones represent the progradation of deltas across the Visean and early Namurian basins. The western, deepest part of the Widmerpool Trough was inverted and partially eroded by the Late Carboniferous inversion during the Variscan orogeny prior to deposition of Permo-Triassic rocks.

For the experiments described below, the dark grey shale core was crushed and sieved to between 2 and 5 mm chips (2 mm minimum and 5 mm maximum particle size), which were subsequently thoroughly mixed to obtain a homogeneous sample. A high pressure water pyrolysis (HPWP) experiment was carried out at 800 bar using a 25 ml Hastelloy cylindrical pressure vessel rated to 1400 bar at 420 °C as previously described in detail (Uguna et al., 2012, Uguna et al., 2015; Whitelaw et al., 2019). In this case, the sequential HPWP experiment was carried out to mimic successive periods of burial and uplift during source rock maturation under natural conditions or the impact of a periodic wet combustion process during hydrothermal treatment in

Table 1
Mineralogical composition of the initial Rempstone Shale (whole rock).

Mineral (%)					
Silicates	Carbonates		Clay		Sulphide and sulphate
Quartz	Siderite	Mica	Kaolinite	Chlorite	Pyrite
34.5	3.0	35.8	24.6	1.9	0.2

shale reservoirs. The initial shale rock (19 g) was first heated at 350 °C for 24 h, and at the end of the run the experiment was stopped and allowed to cool to ambient temperature, before the generated products (gas, expelled oil and pyrolysed rock) were recovered, and the pyrolysed rock dried in an oven at 40 °C overnight to remove surface water.

Initially vacuum was not used for drying to avoid removing pore water present in the rock, which was intended to be left in the shale pore network during some other characterisation experiments (not described here) of the pyrolyzed shales. After drying the rock, about 3 g of the rock was put aside for further analysis, and the rest re-heated. The process was repeated by heating the same rock sample successively at 380 °C for 24 h, 420 °C for 24 h, 420 °C for 48 h, and finally 420 °C for 120 h. The experiments were stopped after every heating stage and the products recovered until the final run at 420 °C for 120 h. It is important to note that no expansion of the shale chips was observed at any stage of the pyrolysis (hydrothermal treatment) process. Table 1 presents the mineralogical composition of the initial Rempstone whole rock shale obtained from XRD analysis. The silicate mineral present was quartz, the carbonate mineral was siderite, and the clay minerals were kaolinite and chlorite. Although mica was detected in the whole rock sample under clay minerals, the XRD was unable to determine the composition/type of the mica, as mica is a metamorphosed form of clay mineral. The sulphide and sulphate mineral present was pyrite.

Table 2 shows the TOC and Rock Eval pyrolysis data for the initial and pyrolysed shales obtained from Rock Eval pyrolysis. The Rock Eval pyrolysis was conducted on non-extracted whole rock samples, as previously described in detail (Uguna et al., 2016). A constant reduction in TOC and HI (hydrogen index) was observed after the first stage (initial shale pyrolysis at 350 °C for 24 h) all through to the final stage at 420 °C for 120 h. The constant reduction in both the TOC and HI was due to hydrocarbon (oil and gas) generation during the HPWP experiments. The T_{max} increased constantly from 436 °C for the initial shale to 605 °C after pyrolysis at 420 °C for 120 h. The steady increase in T_{max} with increase in temperature and time is due to source rock maturation occurring during hydrocarbon generation, consistent with natural geological conditions.

2.2. Integrated gas sorption and mercury porosimetry

The nitrogen adsorption/desorption isotherms were measured at liquid nitrogen temperature (77 K) using a Micromeritics ASAP 2020 physisorption analyser. Adsorption was measured over the relative pressure (P/P_o) range of 0.01–0.995 for adsorption and desorption from 0.995 to 0.10 P/P_o. The equilibration times used were 20 s and 60 s. Two different times were tested to ensure that the sample isotherm was fully equilibrated. The samples were outgassed at 140 °C for 2 h under vacuum prior to analysis. Mercury intrusion and retraction curves were measured using a Micromeritics 9520 AutoPore mercury porosimeter over the pressure range of 0.0013–414 MPa covering a pore diameter range of 300 μm to 3.6 nm respectively.

For integrated experiments, a full adsorption-desorption isotherm was measured after which the sample was retrieved and transferred to the mercury porosimeter. Mercury intrusion data was generated for the range specified above followed by retraction back down to atmospheric pressure. Once the mercury porosimetry experiment was finished the sample was immediately discharged from the sample cell, recovered and returned to the physisorption sample cell. Once in position on the instrument analysis port, a dewar of liquid nitrogen was immediately raised around the sample to freeze the mercury within the pores in which it had been entrapped. It is important to do this immediately following the mercury porosimetry run to prevent the possibility of mercury "bleeding" from the pore network with time. The sample was left for approximately 30 min to ensure all the mercury within the sample had frozen solid after which the sample was evacuated to less than 5 μm Hg and held under vacuum for 30 min. A second isotherm was then measured using the same parameters as the first. Previous work (Nepryahin et al., 2016; Rigby, 2018) has shown that the mercury ganglia in partially saturated samples do not migrate during repeated freeze-thaw cycles.

Table 2
Rock Eval and total organic carbon (TOC) data for initial Rempstone, samples heated at the beginning of each stage of HPWP and residues obtained after each stage.

Sample	Before each HPWP stage			After each HPWP stage		
	TOC (%)	HI (mg/g)	T_{max} (°C)	TOC (%)	HI (mg/g)	T_{max} (°C)
Initial shale	6.69	413	436	–	–	–
350 °C, 24 h	6.59	413	436	5.95	254	444
380 °C, 24 h	5.95	254	444	4.78	65	459
420 °C, 24 h	4.78	65	459	4.56	16	580
420 °C, 48 h	4.56	16	580	4.45	8	600
420 °C, 120 h	4.45	8	600	4.56	6	605

2.3. Overcondensation

The overcondensation experiments were carried out on a Micromeritics ASAP 2020 physisorption analyser using a method similar to that described by Murray et al. (1999). In the overcondensation experiment, the first stage is to increase the pressure in the sample tube to higher than the saturated vapour pressure of nitrogen. This pressure increase should facilitate sufficient condensation such that even the biggest pores are filled with liquid nitrogen at the start of the overcondensation desorption isotherm, which will probably inevitably also involve some bulk condensation in the sample tube. This bulk condensation is what is avoided in the conventional experiment. The required period to reach this stage is dependent upon the sample size and the pore volume. While it does not matter if the volume of condensate is much higher than that needed for complete pore filling, the total duration of the experiment would be much longer in that case. Once complete pore-filling had been achieved, the pressure was lowered to just below the saturated vapour pressure of nitrogen such the bulk condensate vaporized completely while keeping all the sample internal porosity liquid-filled. Once this stage has been accomplished, the first data point on the overcondensation desorption isotherm can be measured. This point corresponds to the total pore volume of the sample. The pressure is then progressively lowered in small steps, and the rest of the desorption isotherm was obtained in the usual way.

2.4. Water and cyclohexane adsorption

Experiments were performed on a Surface Measurement Systems DVS Adventure/Resolution instrument. Both water and cyclohexane vapour sorption experiments were carried out on the samples at 25 °C. For both the experimental runs, the samples were initially preheated at 105 °C for 180 min. They were then dried at 0% P/P_o (zero relative humidity) under a continuous flow of dry air at 25 °C for 300 min to establish the dry mass. The samples were then exposed to the following typical partial pressure profile at 25 °C: 0%, 1%, 2%, 3%, 5% and then in a 5% step to 40%. A fixed time of 180 min was selected for each step. The sample uptake versus time was also obtained for each point in the equilibrium isotherms. 180 mins was found to be sufficient to allow full

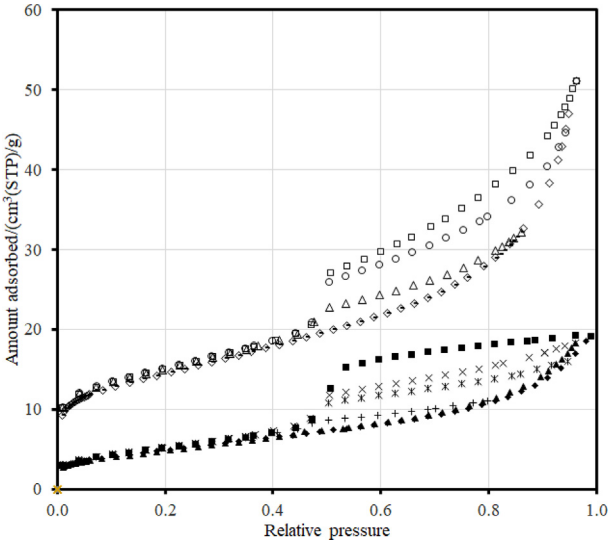

Fig. 1. Nitrogen sorption scanning curves for untreated sample#1 (with adsorption to various ultimate pressures: 0.987 (▲), 0.99 (◆); and desorption from various ultimate pressures 0.86 (+), 0.946 (*), 0.962 (×), and 0.99 (■)) and for treated sample#1 (with adsorption to various ultimate pressures: 0.86 (−), 0.962 (◇); and desorption from various ultimate pressures 0.86 (△), 0.946 (◯), 0.962 (□)).

equilibration of each pressure step.

2.5. Computerised X-ray tomography (CXT)

The sample before and following mercury porosimetry was imaged using a High Resolution X-ray 3D Computed Tomography Microscope Instrument of model VeraXRM-510 (manufactured by Xradia Inc, Pleasanton, CA, USA). The voxel resolution was 3 μm. Typically 2–3 chips of each sample type were imaged. So that data from each type of experiment was mutually consistent, the very same sample was used for the whole series of gas sorption conventional and overcondensation experiments, and mercury porosimetry, and CXT.

3. Results

3.1. Nitrogen sorption

Fig. 1 shows the conventional nitrogen sorption boundary isotherms and some scanning curves for the untreated core chips and the treated sample. It can be seen that the accessible pore volume increases substantially on treatment. It is noted that whereas the hysteresis loop for the untreated sample is parallelogrammatic, that for the treated sample shows a significant curvature. Both sets of isotherms show a sharp knee and desorption step over relative pressures ~0.4–0.5, and this feature is typically attributed to the cavitation phenomenon associated with narrow pore necks of sizes less than ~4 nm guarding access to wider pore bodies. It is noted that the near-vertical desorption step is ~7.5 $cm^3(STP)g^{-1}$ in size in both cases.

It is noted that the scanning curves in Fig. 1 exhibit a variety of forms related to the underlying network architecture. For the untreated sample, the scanning curve to an ultimate relative pressure of 0.946 has a desorption branch that, largely, runs parallel to the initial flat plateau in the boundary desorption isotherm, and crosses directly to a point on the desorption boundary curve riser at a similar adsorbed amount to the initial turning point on the adsorption branch. However, in contrast, the scanning curve to an ultimate relative pressure of 0.962 shows a sharp decline in adsorbed amount as soon as the pressure is reversed at the higher turning point, and then flattens out and intersects the boundary desorption riser at almost the same place as the 0.946 relative pressure curve. This difference in behaviour suggests differences in network morphology between pores that fill below relative pressures of 0.946, and those that fill in the range 0.946–0.962.

Models for the proposed pore network morphologies are shown schematically in Fig. 2. In the scanning curve to 0.946 the pore neck B would fill at low pressures and the much wider pore body A would fill on the adsorption branch at relative pressures above 0.8. However, the extreme narrowness of the neck B would mean that, on desorption, the nitrogen pressure would decrease to the point where cavitation occurs, and all the condensate evaporates in the steep desorption step at relative pressures ~0.5–0.4. In contrast, for the scanning curve up to 0.962, very narrow pore neck C would fill at very low pressure, while the medium sized pore body E would fill at relative pressures between 0.946 and 0.962 corresponding to those required for a hemispherical

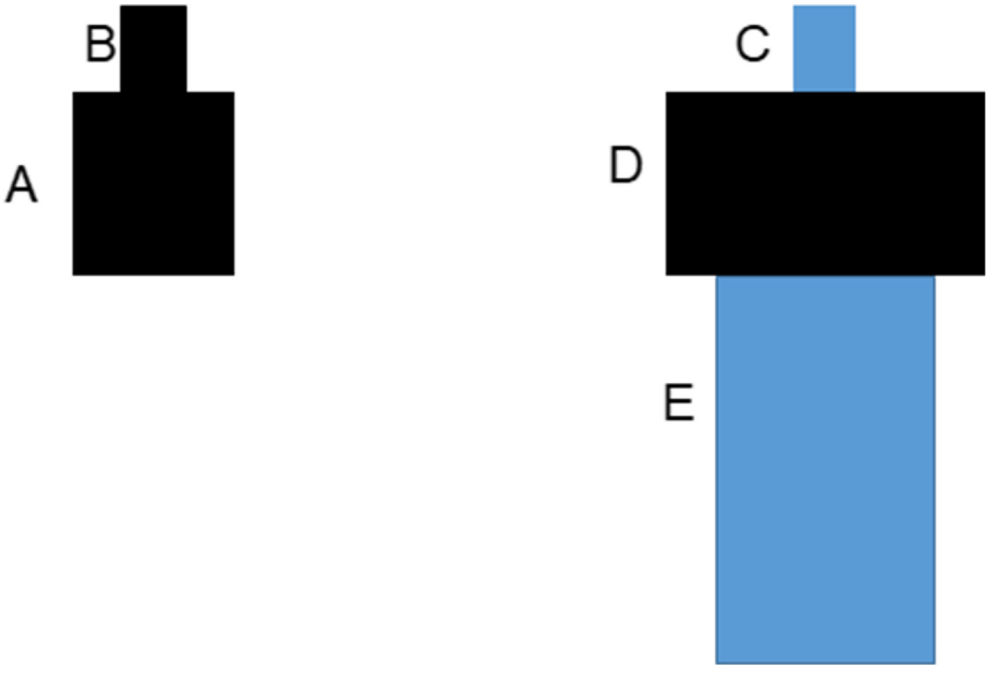

Fig. 2. Schematic diagram of models for the proposed pore network morphologies, as described in the main text, used to interpret the scanning curve data in Fig. 1. The black colour represents empty pores, and the blue colour represents those pores that would fill with condensate at the top of a scanning curve up to an ultimate pressure of 0.962, as described in the main text. (For interpretation of the references to colour in this figure legend, the reader is referred to the Web version of this article.)

meniscus since E has a dead-end. The very large pore body D would only fill at relative pressures above 0.962. If the adsorption process is reversed at relative pressure 0.962 then D would remain empty of condensate and the condensate in E could evaporate via a hemispherical meniscus into the vapour-filled D as soon as the pressure change direction is reversed. If the adsorption process continues up to higher pressures than 0.962 then D would then fill with condensate meaning the only free meniscus with vapour is at the mouth of C, which would now control the desorption. If C is very narrow the pressure would decline below that for cavitation to occur in D and E together at relative pressures ~0.5–0.4. Hence, the scanning curve reveals the presence of two types of network architecture in the untreated shale.

The hysteresis loop for the treated shale is of a very different shape to that of the untreated shale. Instead of the near horizontal form of the initial untreated desorption boundary curve, the corresponding curve for the treated sample has more Type II isotherm character. It is suggested that the form of the treated isotherms is consistent with them being a composite of the original untreated isotherm and a Type II isotherm resulting from multi-layer adsorption and capillary condensation in a new set of large macropores. In order to test this hypothesis the 0.962 relative pressure scanning curve data for the treated sample was fitted to a composite, homotattic patch model (Walker and Zettlemoyer, 1948) isotherm consisting of the desorption boundary curve plateau for the untreated sample and a Frankel-Halsey-Hill isotherm, and the results are shown in Fig. 3. The statistical quality of the fit was very good with a coefficient of determination of 0.9937.

The initial reversible sections (relative pressures 0.0096–0.4) of the nitrogen adsorption isotherms for untreated and treated shale samples were fitted to a homotattic patch model (Walker and Zettlemoyer, 1948) consisting of two types of patches with Langmuir and fractal BET isotherms (Mahnke and Mögel, 2003). The parameters obtained from the fits in Fig. 4 are shown in Table 3. It can be seen that the fitted parameters mean that the forms of the fitted components are close to the Henry's law limit for the Langmuir component, and the Langmuir limit for the fractal BET component. In addition, also shown in Table 3 is the specific surface area calculated from this model assuming the standard cross-sectional area for adsorbed nitrogen (0.16 nm^2). The total specific surface area obtained for the untreated sample from the homotattic patch model, given in Table 3, is higher than that obtained from the standard single-component BET model of 17.7 ± 0.7 m^2g^{-1} (with BET constant = 79.7). However, the standard BET model was only applied to the ISO recommended, more limited, fitting range of

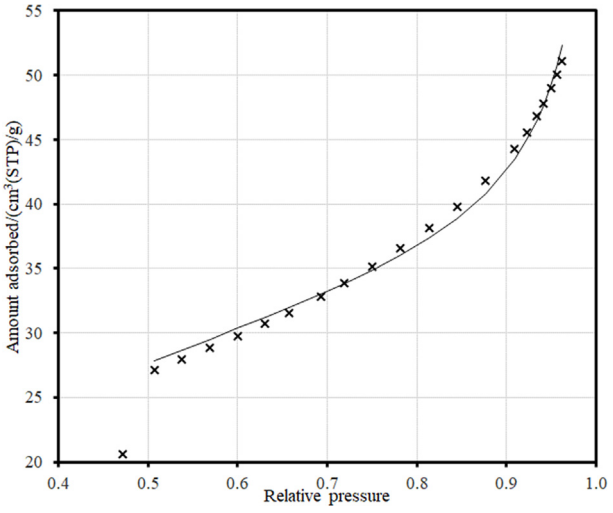

Fig. 3. Desorption scanning curve from relative pressure of 0.962 for the treated sample#1 (×) and fit (solid line) of these data to a composite, homotattic patch model consisting of the desorption boundary curve plateau for the untreated sample and a Frankel-Halsey-Hill isotherm.

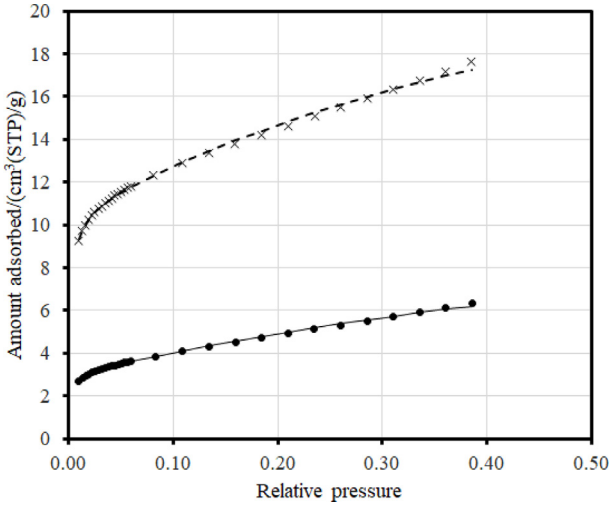

Fig. 4. Nitrogen adsorption isotherms (symbols) and fits of Langmuir and fractal BET homotattic patch models (lines) for untreated (●, solid line) and treated#1 (× , dashed line) samples.

relative pressures from 0.05 to 0.3 (ISO, 2010). Hence, the homotatttic patch model is consistent with a significantly larger portion of the isotherm data-set. It can be seen that the thermochemical treatment results in an increase in specific surface area according to nitrogen from 62 to 130 m^2g^{-1}. The fitted BET constant and fractal dimension are such that the BET component approximates a Henry's law type behaviour in this range. This is consistent with the visual appearance of the isotherms which suggests linear behaviour above the first knee at low pressure until the hysteresis closure point.

3.2. Overcondensation

In order to further test the hypothesis that thermochemical treatment results in the creation of an additional network, rather than modifying the original, the overcondensation method was used to overcome the limitations in the ultimate pressure possible with a conventional adsorption experiment. Fig. 5 compares the nitrogen sorption isotherms for a treated shale sample obtained by the conventional method and by the overcondensation method. The overcondensation curve exhibits a vertical drop in amount adsorbed at a relative pressure of 1 as condensate evaporated from the bulk phase surrounding the sample. Once only the sample porosity is filled with condensate the overcondensation curve deviates from the vertical and forms the boundary desorption isotherm for a pore-filled sample. From Fig. 5, it can be seen that the ultimate amount adsorbed is much higher on the overcondensation isotherm than it is for the conventional isotherm(s). This is because the conventional method truncates the adsorption process before the sample porosity is completely filled with condensate. In order to check that the larger amount adsorbed at the top of the overcondensation boundary desorption isotherm, compared to the conventional adsorption isotherm(s), was not due to the latter not reaching equilibrium, due to kinetic limitations, the conventional isotherm was obtained twice at an equilibration time of 20 s (in order to check inter-experimental variability) and again at an equilibration time of 60 s. From Fig. 5, it can be seen that the equilibration time for the conventional isotherm does not make a significant difference to the ultimate amount adsorbed at the highest relative pressure, especially compared with the much larger amount adsorbed at the top of the overcondensation desorption boundary curve. Hence, the difference in adsorbed amounts between conventional and overcondensation experiments is not due to the former not being properly equilibrated due to kinetic limitations.

From Fig. 5 it can also be seen that the overcondensation boundary

Table 3
Parameters obtained for two-component (Langmuir and fractal BET) homotattic patch model fits to nitrogen adsorption isotherms for untreated and treated#1 shale sample shown in Fig. 4.

Sample	Fraction of Langmuir component	Langmuir constant	BET constant	Fractal dimension	Specific surface area/(m^2g^{-1})
Untreated	0.791	1.0	674.6	3.0	62.2
Treated	0.652	1.4	644.8	3.0	130

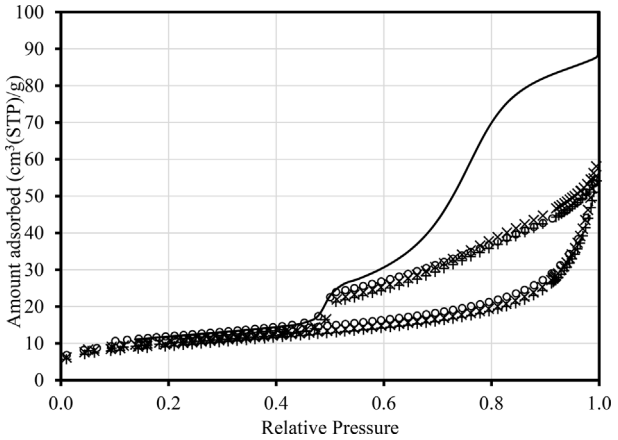

Fig. 5. Nitrogen sorption isotherms for the treated shale sample#2 obtained by the conventional method using an equilibration time of 20 s (repeats ◯ and ×) and 60 s (+), and by the overcondensation method (solid line).

desorption isotherm exhibits two steps, including a larger, more rounded one at relative pressure ~0.9–0.7, and a smaller, steeper step at relative pressure ~0.5–0.4. This suggests two separate regions of the network with different desorption transitions. The desorbed gas volume from the first step (from ~88.4 to 26.1 cc(STP)g^{-1}), at high pressure, was converted to a pore volume assuming the adsorbed phase was liquid nitrogen at its normal boiling point, and the value obtained was 0.0965 ml g^{-1}. The point of inflexion of the first big desorption step occurs at a relative pressure of ~0.73. From the method of Broekhoff and De Boer (1968), the pore radius is ~5 nm.

In order to further study the structure of the network that developed with thermochemical treatment, scanning curves/loops were performed from the overcondensation boundary desorption isotherm for another sample of treated shale. Fig. 6 shows both the ascending adsorption scanning curve and descending desorption curve for two separate scanning loops starting on the overcondensation boundary desorption isotherm at two different relative pressures of ~0.6 and ~0.8, which

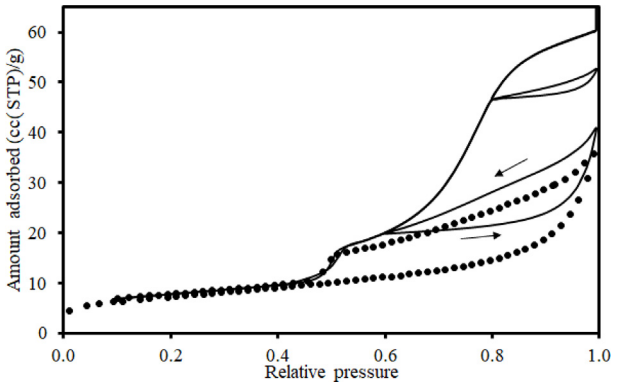

Fig. 6. Ascending adsorption scanning curves (starting at relative pressures of 0.6 and 0.8) and corresponding descending desorption curves (indicated by descending arrow) for scanning loops starting on the overcondensation boundary desorption isotherm (solid line), and conventional isotherms for treated sample#3 (●).

both are above the final step down. It can be seen that both the ascending adsorption scanning curves cross, more or less, horizontally for a large fraction of the hysteresis width to the boundary adsorption isotherm, with only a slight significant upturn just before each joins the anticipated path of the adsorption boundary curve, which they then follow. Crossing scanning curves are more typically associated with the narrow hysteresis for boundary isotherms arising from isolated, cylindrical pore systems like SBA-15 silica, rather than the very broad hysteresis for the thermochemically-treated shale sample. The desorption scanning curves both show some desorption occurring immediately after the direction in the change in pressure is reversed, which continues across the hysteresis width, and the lower curve is similar in form, and parallel in path, to the desorption isotherm for the conventional sorption experiment. The conventional desorption experiment is essentially just a descending scanning curve from the partial adsorption boundary curve.

3.3. Water and cyclohexane adsorption

Fig. 7 compares the single component adsorption isotherms obtained for water and cyclohexane on samples of the untreated and treated shale. It is noted that the first knee (Point B) is more pronounced for cyclohexane than for water. The isotherm data-sets were each fitted to the single-component fractal BET model, and the parameters thus obtained are shown in Table 4. The specific surface areas were calculated from the fitted monolayer capacities using a cross-sectional area of 0.106 nm^2 for water and 0.264 nm^2 for cyclohexane, and these are also shown in Table 4. It is noted, first, that the specific surface area of the untreated sample from water adsorption exceeds that obtained from the standard nitrogen BET method mentioned above. Second, it can be seen that the total of the cyclohexane and water specific surface areas added together for the untreated sample, of ~60 m^2g^{-1}, is very similar to the specific surface area obtained from nitrogen via the homotattic patch model. Further, the micropore contribution, from the Langmuir component of the nitrogen adsorption homotattic patch model, for the untreated sample of 49 m^2g^{-1} is similar to the water specific surface area of 43.4 m^2g^{-1}, and the mesopore contribution from the nitrogen fractal BET component of ~13 m^2g^{-1} is similar to the cyclohexane surface area of 16.5 m^2g^{-1}. These findings suggest that water can access the same microporosity accessed by nitrogen in the untreated sample, but the mesoporosity is relatively hydrophobic (Type III isotherm behaviour) and only accessed by the cyclohexane, which, in turn, may be too big to access the microporosity. Relatively low adsorption of water is associated with a lack of polar or polarisable surface groups.

In contrast, the total specific surface area from both water and cyclohexane combined for the sample after treatment of ~71 m^2g^{-1} is not much larger than before treatment, and thus much smaller than that suggested by nitrogen sorption of ~130 m^2g^{-1}.

It can also be seen that, both before and after thermochemical treatment water and cyclohexane give similar surface fractal dimensions, but this is much lower than that obtained from nitrogen. Water and cyclohexane suggest that the surface fractal dimension of the surfaces they each probe declines after thermochemical treatment. A decrease in fractal dimension suggests the surface becomes less rough. This may suggest thermochemical treatment does not produce small length-scale defects and may result in some graphitisation of carbon

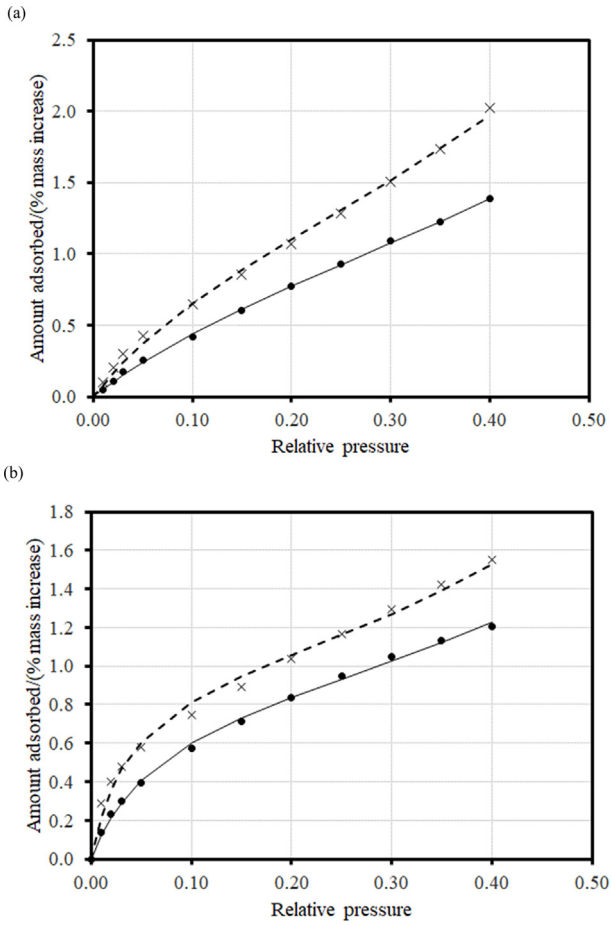

Fig. 7. Water (a) and cyclohexane (b) adsorption isotherms measured at 25 °C for untreated (●) and treated (×) samples. The lines shown are fits of the fractal BET model to the data for untreated (solid line) and treated (dashed line) samples.

Table 4
Parameters obtained from single component fractal BET model fits to water and cyclohexane adsorption isotherms for untreated and treated samples shown in Fig. 7.

Sample	Adsorbate	BET constant	Fractal dimension	Specific surface area/(m^2g^{-1})
Untreated	Water	4.44	2.18	43.4
Untreated	Cyclohexane	15.38	2.15	16.5
Treated	Water	5.93	2.00	52.6
Treated	Cyclohexane	28.27	2.00	18.2

present, as graphite sheets are flat. In contrast, the BET constants for each adsorbate increase following thermochemical treatment of the shale, though this increase is much more substantial for cyclohexane. This finding would be consistent with the production of more graphitised carbon surfaces during treatment, as graphite surfaces are both flat and attractive to cyclohexane as a non-polar adsorbate.

The combined results from the adsorption experiments for three adsorbates suggest the surface properties of the porosity formed with thermochemical treatment are largely different to those of that existing beforehand.

3.4. Integrated gas sorption and mercury porosimetry

Following the nitrogen sorption experiment on the treated sample, a mercury porosimetry experiment was also carried out on the same sample. The raw mercury porosimetry data analysed using the Kloubek (1981) correlations are given in Fig. 8. From Fig. 8, it can be seen that ~75% of the intruded mercury becomes entrapped in the sample. It is noted that the pore volume corresponding to the first large step at high pressure in the nitrogen overcondensation desorption boundary curve was ~0.0965 ml g^{-1}, which is similar to the intruded volume for mercury porosimetry. The residual discrepancy is probably due to the neglect of the remaining multi-layer adsorption still present at the bottom of the desorption step in the pores where the pore core has emptied of condensate. Since it is unlikely mercury can enter the mesopores that empty of gas condensate by cavitation because the necks guarding them are too small, these findings suggest the nitrogen overcondensation and mercury intrusion probe the pore network created by thermochemical treatment. The pore radius corresponding to the point of inflexion in the mercury intrusion curve is ~5–6 nm, similar to that for the nitrogen overcondensation desorption step.

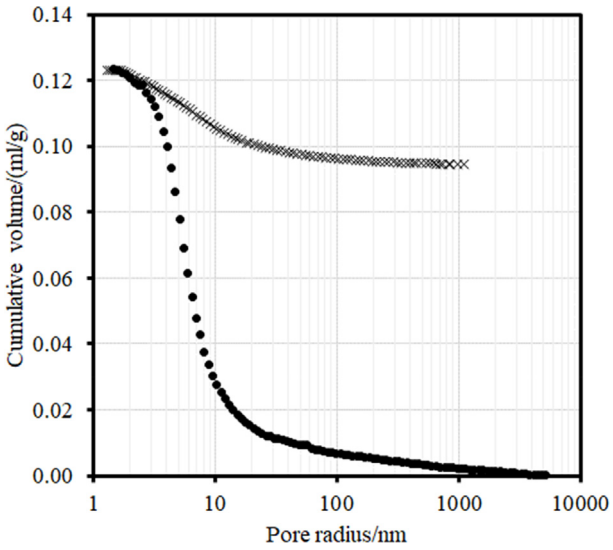

Fig. 8. Mercury intrusion (●) and extrusion (×) curves for treated shale sample#2 analysed using Kloubek (1981) correlations.

Following the mercury porosimetry experiment, conventional and overcondensation nitrogen sorption experiments were conducted on the same sample containing entrapped mercury. Fig. 9 compares the results from conventional nitrogen sorption experiments for untreated and treated shale samples with that for the treated sample following

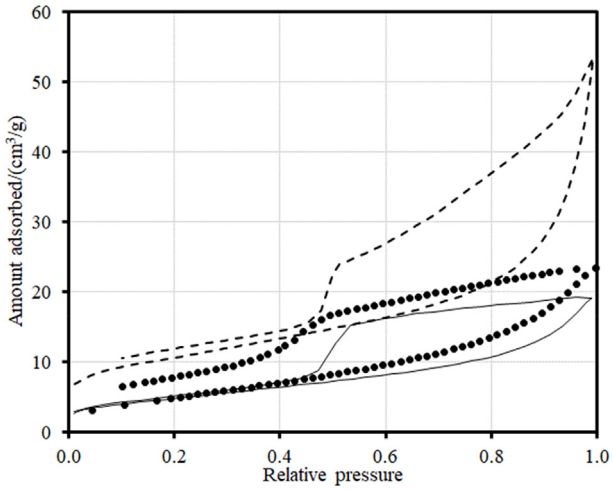

Fig. 9. Nitrogen sorption isotherms for untreated sample before mercury porosimetry (solid line), and for treated sample#2 before (dashed line) and after (●) mercury porosimetry.

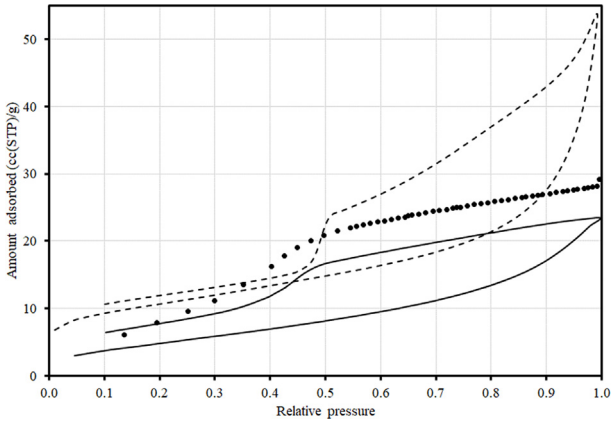

Fig. 10. Conventional nitrogen sorption isotherms for treated sample#2 before (dashed line) and after (solid line) mercury porosimetry, and nitrogen overcondensation boundary desorption isotherm after mercury porosimetry (●).

mercury entrapment. It is noted that, after porosimetry, there is still adsorption in the low pressure range, which is, thus, due to the pores that remain empty after mercury entrapment. The part of the pore network that is shielded by the necks that give rise to a cavitation step in desorption cannot be intruded with mercury because these necks are generally too small for mercury to enter. It can also be seen that the position and form of the nitrogen sorption isotherms for the treated sample after porosimetry are very similar to those for the untreated sample.

Fig. 10 shows a comparison of the conventional nitrogen sorption isotherms before and after mercury entrapment in the treated sample with the overcondensation desorption isotherm for the treated sample after mercury entrapment. It can be seen from Fig. 10 that the amount of macropore volume missed by the conventional experiment is relatively small for the sample following mercury entrapment. These data suggest that the mercury entrapment predominantly occurs in the pore network generated by the thermochemical treatment.

In addition to equilibrium isotherms, kinetic uptake data was acquired for pressure points at the low pressure end of the nitrogen isotherm, where the treated sample was virtually empty of adsorbate, before and after mercury entrapment. The experimental data were fitted to the Linear Driving Force model (LDF) (Nepryahin et al., 2016). In the LDF model, the key fitting parameter is the mass transfer coefficient, which is proportional to the intrinsic pore network diffusivity of the rock. An example of an uptake curve and fit to the LDF model is shown in Fig. 11. The fitted mass transfer coefficient was corrected for adsorption, and the corrected mass transfer coefficients for both samples are shown in Table 5. It can be seen that the adsorption-corrected

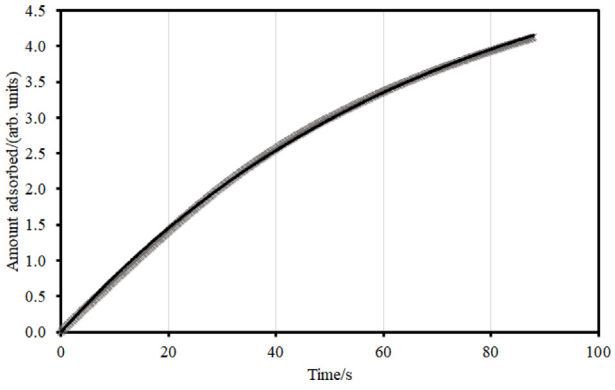

Fig. 11. Example of nitrogen gas uptake data (×) for treated sample before mercury entrapment, and fit of these data to the Linear Driving Force model (solid line).

Table 5
Adsorption corrected mass transfer coefficients for nitrogen in dry treated shale samples.

Sample	Mass transfer coefficient/s^{-1}
Treated after mercury entrapment	1×10^{-6}
Treated before mercury entrapment	0.001

mass transfer coefficient declines by a factor of ~1000 following mercury entrapment. This suggests that the pore network where the mercury becomes entrapped is critical to mass transport.

3.5. Computerised X-ray tomography

CXT images were obtained for typical samples of untreated shale chips, and treated shale chips from before and after mercury porosimetry experiments, and examples of 2D image slices are shown in Fig. 12. In the images the brighter white pixels correspond to high x-ray absorbance, and thus high density, whereas darker blacker pixels correspond to low x-ray absorbance and low density. From Fig. 12(a), it can be seen that the shale matrix is typically mid-grey but contains some white speckles, and dark dots and lines. It is likely that the white speckles are iron pyrites because these would have high x-ray absorbance. The thin black lines and dots are probably cracks and voids. The fatter dark regions are low x-ray absorbing carbon (which has been confirmed by elemental analysis of electron microscopy data, which will be presented below). It is noted from the CXT image of the treated sample in Fig. 12(b) that the number and size of the cracks and voids has increased dramatically following thermochemical treatment. From the CXT image(s) of the treated sample following mercury porosimetry, it can be seen that the bright white, high x-ray absorbance features increase in prevalence and size dramatically compared to the untreated sample. This is likely to be due to the entrapped mercury. It can be seen that the large voids evident in Fig. 12(b) have largely become filled with mercury, as have the cracks. There are also many more bright white specks through the sample.

Fig. 13 shows 3D reconstructions of the entrapped mercury distribution in a treated shale chip. It can be seen that the macroporosity occupied by the entrapped mercury is pervasively distributed through the chip. The gated 2D images show extensive long fingers of entrapped mercury suggesting the macropores provide easy mass transport over extended distances.

3.6. Electron microscopy

SEM images of both untreated and treated samples, such as the example given in Fig. 14, were obtained. These images show several irregular black shapes.

Elemental mapping results, such as those shown in Fig. 15, suggest that the black shapes observed in the micrographs are almost completely composed of carbon, and contrast in chemical composition to other tested locations, and thus are the remains of organic matter. For treated samples, the SEM images, such as that shown in Fig. 16, show that some of the carbon particles develop smooth ovoid features that look like bubbles. It is suggested that these may be the result of rapid vapourisation of volatile organic components during treatment.

4. Discussion

Gas sorption scanning data has shown the complexity, but also revealed the structure, of the original void space of the untreated shale rock (as shown in Fig. 2). However, the conventional sorption scanning curve and overcondensation data also suggest that another, additional pore network is developed upon thermochemical treatment. The appearance of two separate percolation steps in the boundary desorption

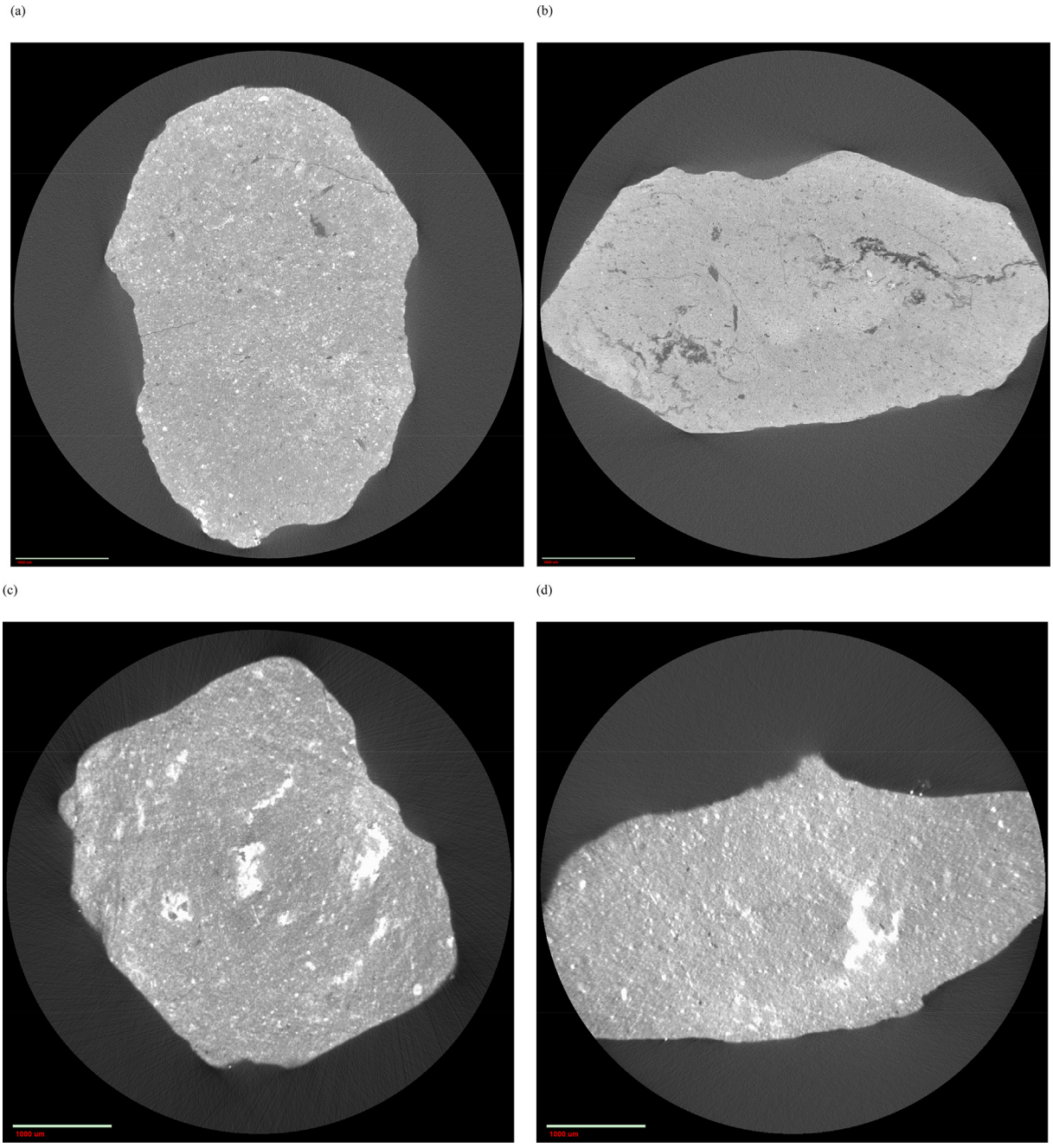

Fig. 12. 2D CXT image slices through typical samples of (a) untreated shale chip, (b) treated shale chip, and (c&d) treated shale chips after mercury porosimetry (from sample #2). The scale bars shown represent 1000 μm.

isotherm for the overcondensation data suggests that exterior access occurs via two separate routes for the old and new porosity. While the form of the ascending scanning curve from the boundary desorption isotherm in the overcondensation experiment is crossing, the hysteresis width is much larger than would be expected from the Cohan (1938) equations for isolated cylindrical pores. This suggests the void space may have the form presented in Fig. 17(a). In this model void space, very narrow windows guard access from the exterior to narrow necks and larger bodies. When the void space is full of liquid condensate desorption is controlled by the narrow windows. However, on adsorption, the initial condensation pressure is controlled by the wider neck size, which is larger than the window. If adsorption proceeds such that only the neck fills, then, on reversing the direction of the pressure change again, the still empty larger body provides a vapour pocket into which desorption from the neck could occur via a hemispherical meniscus. This hemispherical meniscus would be bigger than the one in the window, and thus desorption would be at a higher pressure than via the window. Hence, desorption could occur sooner than on the boundary desorption isotherm. If the void space has the form of that shown in Fig. 17(b) then desorption on the boundary curve would also be controlled by the narrow window A, but initial adsorption would be controlled by the diameter of Pore C. If larger pore B remains unfilled then adsorption in pore C would be reversible since it is a dead-end pore, and so desorption could commence immediately on reversing the pressure from the boundary adsorption isotherm. Hence, the type of structure given in Fig. 17(b) may give rise to the shape of the scanning curves in Fig. 6.

It is noted that the above electron micrographs (see Fig. 16) suggest large macroporous, bubble-like pores have appeared in the carbonaceous regions in the treated shale sample. The micrographs also suggest

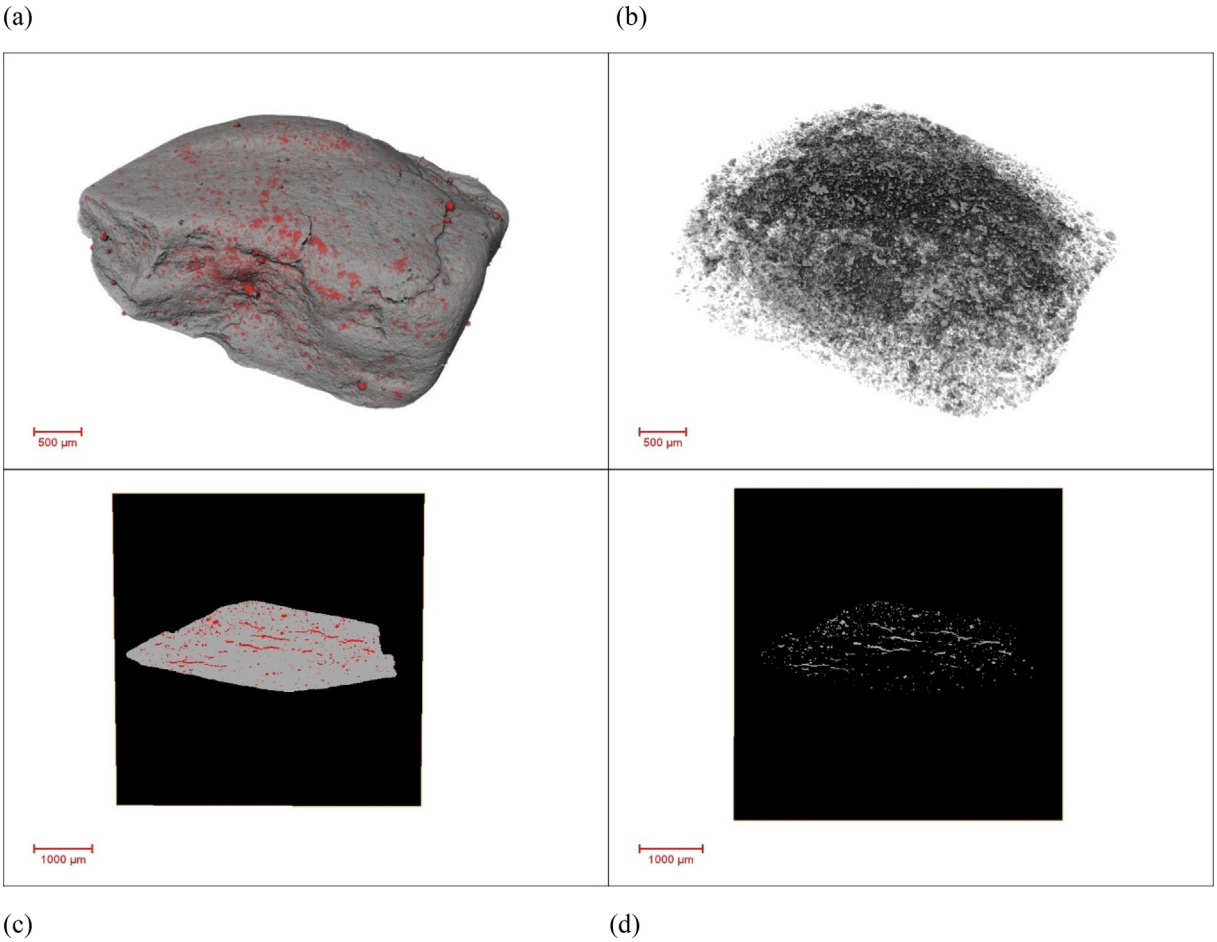

Fig. 13. (a) 3D CXT reconstruction of a treated shale chip following mercury porosimetry. The near-surface entrapped mercury within the chip is shown in red. (b) Full 3D distribution of entrapped mercury within the shale chip. (c) Gated 2D CXT reconstructed slice showing entrapped mercury in red and shale matrix as grey, and (d) 2D spatial distribution of entrapped mercury for the same 2D slice as shown in (c). (For interpretation of the references to colour in this figure legend, the reader is referred to the Web version of this article.)

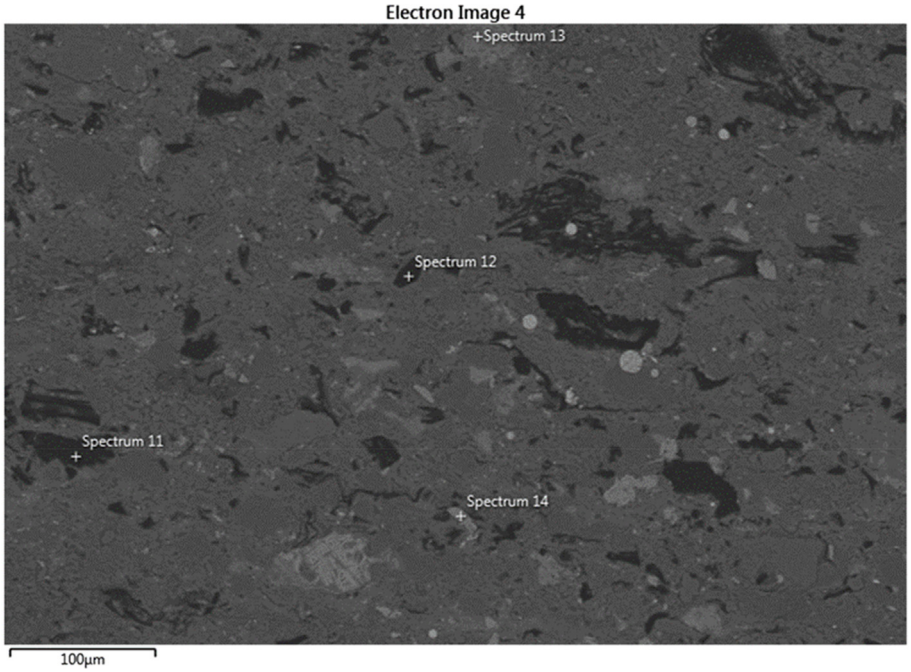

Fig. 14. Typical SEM of polished section of untreated shale sample. The '+' symbols indicate the positions at which the elemental compositional spectra shown in Fig. 15 were obtained.

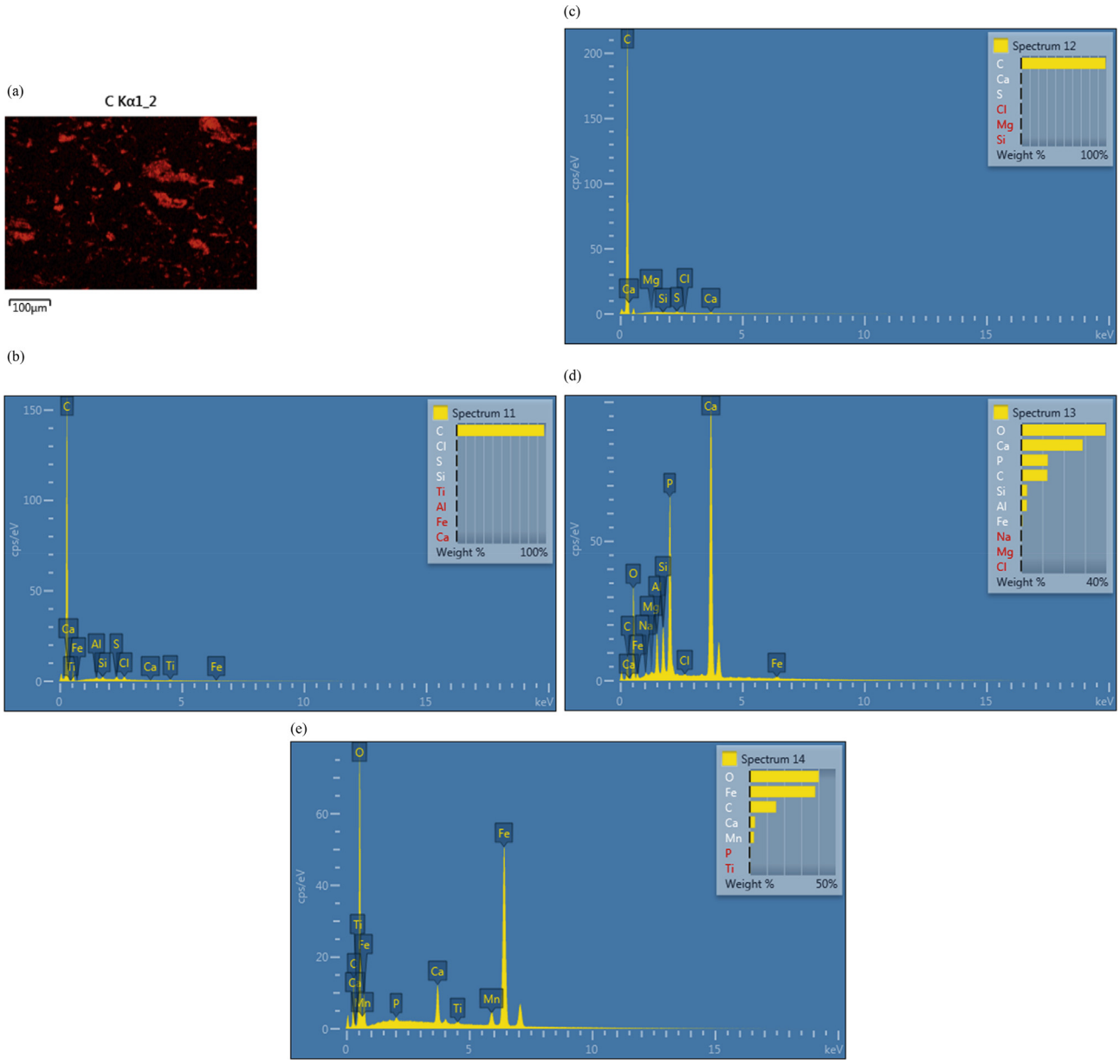

Fig. 15. (a) Elemental mapping of carbon (red phase) for the SEM image shown in Fig. 14, and elemental compositional spectra (b)–(e) obtained at the locations shown in Fig. 14. (For interpretation of the references to colour in this figure legend, the reader is referred to the web version of this article.)

that ovoid bubble pores intersect each other and the boundary of the carbonaceous regions, and, thereby, probably form windows, as can be seen in the image. While the particular carbonaceous region shown in Fig. 16 appears isolated, the image is only two-dimensional and neglects potential connections in the third dimension. Hence, the windows in the ovoid pores, or networks of these, might adjoin the boundary of the sample, in a similar fashion to the model porosity shown in Fig. 17. Carbon bubble pores may also be shielded by inorganic matrix pores. A more detailed EM study will be the subject of a future work.

The mercury porosimetry curves suggest that most of the pores penetrated by mercury become filled with entrapped mercury on extrusion. In contrast, if the high mercury pressure had, instead, crushed the sample inelastically, then the reduction in sample volume would have manifested as apparent mercury entrapment. However, the presence of pervasive entrapped mercury seen in the CXT images in Figs. 12 and 13 suggests that mercury, indeed, intruded the void space, rather than crushed it. There was also no observed change in sample volume following porosimetry.

The integrated gas sorption and mercury porosimetry data for the treated sample showed that the gas sorption isotherms obtained after entrapment very closely resembled the isotherms obtained for the untreated sample. This suggested that the mercury predominantly became entrapped within pores newly created by the thermochemical treatment. The type of pore structures proposed for the new porosity from the overcondensation gas sorption scanning curves shown in Fig. 17 possess the narrow entrance windows known to give rise to high mercury entrapment (Wardlaw and McKellar, 1981). The comparison of the rate of uptake of gas before and after mercury entrapment in the treated sample showed that the pores filled with mercury were critical for mass transport, since their loss led to a decline in rate by a factor of ~1000. The thermochemical treatment thus rendered the shale much more significantly permeable. The original porosity remained only accessible via very small necks less than ~4 nm in diameter, thus making mass transport very difficult.

The CXT data revealed the source of the new porosity. The CXT data

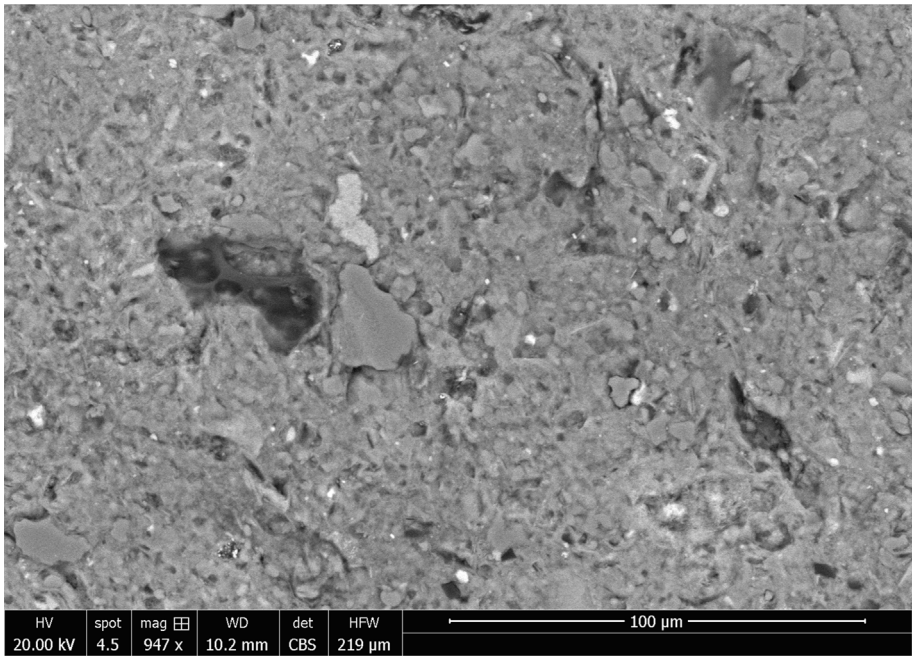

Fig. 16. SEM image of a region of a treated shale sample containing carbon particles.

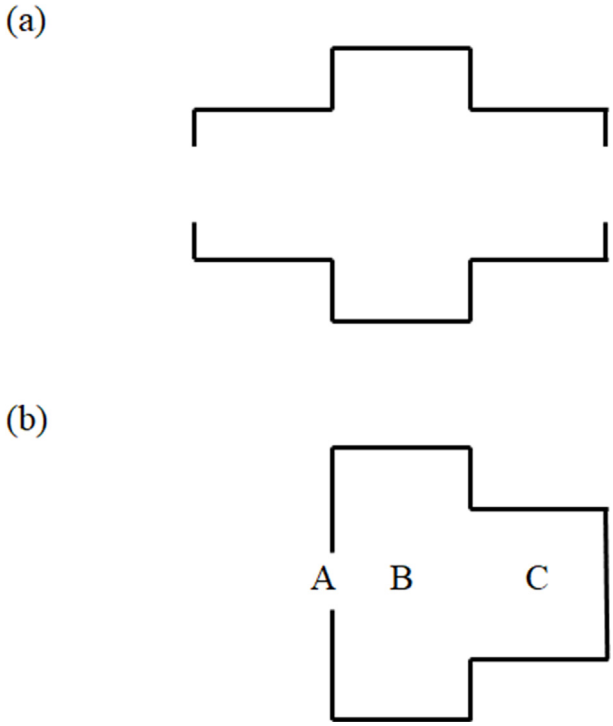

Fig. 17. Schematic diagram depicting model pore structures for interpreting overcondensation experiment scanning curves on treated sample.

suggested that large voids and cracks developed following thermochemical treatment. The CXT images taken after mercury entrapment allowed the mapping of the pervasiveness of the new porosity even for pore sizes below the resolution of the CXT since the x-ray absorbance of entrapped mercury acts as a tracer for the presence of such pores. As shown in previous work (Nepryahin et al., 2016), mercury porosimetry scanning curves can be used to isolate mercury entrapment to pores of a particular size range to image, if desired.

A future work will consider the mechanisms of the formation of the new porosity. For example, during heating, the shale should lose fluid on account of chemical reactions, and this fluid, under experimental conditions, will tend to generate its own porosity and fracture networks.

5. Conclusions

Thermochemical treatment of Bowland shale samples leads to the generation of an entirely new meso-macro-pore network. It has been shown that the overcondensation method extends the capabilities of gas sorption to study this sort of macroporosity. While gas overcondensation scanning curves revealed that the entrances to the new pore network are guarded by narrow necks, combined mercury porosimetry and CXT revealed that the network is highly pervasive. Hence, as demonstrated by integrated rate of gas sorption and mercury porosimetry experiments, these new pores, in particular, lead to a thousand-fold increase in matrix mass transfer coefficient.

Acknowledgements

This work was supported by the Natural Environment Research Council [grant number NE/M00578X/1]. SPR, DJL, and HJ also thank the University of Nottingham for the award of a partial PhD studentship. The authors thank Martin Corfield and Elisabeth Steer (of the Nottingham nmRC) for assistance with acquiring the CXT and SEM data, respectively.

Appendix A. Supplementary data

Supplementary data to this article can be found online at https://doi.org/10.1016/j.marpetgeo.2019.104058.

References

Aukett, P.N., Jessop, C.A., 1996. Assessment of Connectivity in Mixed Meso/macroporous Solids Using Nitrogen Sorption. Fundamentals of Adsorption. Kluwer Academic Publishers, MA, pp. 59–66.

Broekhoff, J.C.P., De Boer, J.H., 1968. Studies on pore systems in catalysts: XIII. Pore distributions from the desorption branch of a nitrogen sorption isotherm in the case of cylindrical pores B. applications. J. Catal. 10, 377–390.

Cohan, L.H., 1938. Sorption hysteresis and the vapor pressure of concave surfaces. J. Am. Chem. Soc. 60, 433–435.

Esparza, J.M., Ojeda, M.L., Campero, A., Dominguez, A., Kornhauser, I., Rojas, F., Vidales, A.M., Lopez, R.H., Zgrablich, G., 2004. N-2 sorption scanning behavior of SBA-15 porous substrates. Colloid. Surf. A Physicochem. Eng. Asp. 241, 35–45.
Fraser, A.J., Gawthorpe, R.L., 1990. Tectono-stratigraphic development and hydrocarbon habitat of the Carboniferous in northern England. In: In: Hardman, R.F.P., Brooks, J. (Eds.), Tectonic Events Responsible for Britain's Oil and Gas Reserves, vol. 55. Geological Society Special Publication No, pp. 49–86.
Fusi, N., Martinez-Martinez, J., 2013. Mercury porosimetry as a tool for improving quality of micro-CT images in low porosity carbonate rocks. Eng. Geol. 166, 272–282.
Glatz, G., Castanier, L.M., Kovscek, A.R., 2016. Visualization and quantification of thermally induced porosity alteration of immature source rock using X-ray computed tomography. Energy Fuels 30, 8141–8149.
Greaves, M., Dong, L.L., Rigby, S.P., 2012. Validation of toe-to-heel air-injection bitumen recovery using 3D combustion-cell results. SPE Reserv. Eval. Eng. 15, 72–85.
ISO, 2010. BS ISO 9277:2010 Determination of the Specific Surface Area of Solids by Gas Adsorption — BET Method. ISO, Switzerland.
Klaver, J., Hemes, S., Houben, M., Desbois, G., Radi, Z., Urai, J.L., 2015. The connectivity of pore space in mudstones: insights from high-pressure Wood's metal injection, BIB-SEM imaging, and mercury intrusion porosimetry. Geofluids 15, 577–591.
Klobes, P., Riesemeie, H., Meyer, K., Goebbles, J., Hellmuth, K.H., 1997. Rock porosity determination by combination of X-ray computerized tomography with mercury porosimetry. Fresenius J. Anal. Chem. 357, 543–547.
Kloubek, J., 1981. Hysteresis in porosimetry. Powder Technol. 29, 63–73.
Leeder, M.R., 1982. Upper Palaeozoic basins of the British Isles-Caledonide inheritance versus Hercynian plate margin process. J. Geol. Soc. Lond. 139, 479–491.
Leeder, M.R., 1988. Recent developments in Carboniferous geology: a critical review with implications for the British Isles and N.W. Europe. Proc. Geol. Assoc. 99, 73–100.
Lin, Q., Al-Khulaifi, Y., Blunt, M., Bijeljic, B., 2016. Quantification of sub-resolution porosity in carbonate rocks by applying high-salinity contrast brine using X-ray microtomography differential imaging. Adv. Water Resour. 96, 306–322.
Liu, H.L., Zhang, L., Seaton, N.A., 1993. Analysis of sorption hysteresis in mesoporous solids using a network model. J. Colloid Interface Sci. 156, 285.
Lore, J.S., Eichhubi, P., Aydin, A., 2002. Alteration and fracturing of silaceous mudstone during in situ combustion, Orcutt field California. J. Pet. Sci. Eng. 36, 169–182.
Mahnke, M., Mögel, H.J., 2003. Fractal analysis of physical adsorption on material surfaces. Colloids Surf., A 216, 215–228.
Matthews, G.P., Spearing, M.C., 1992. Measurement and modelling of diffusion, porosity and other pore level characteristics of sandstones. Mar. Pet. Geol. 9, 146–154.
Matthews, G.P., Ridgway, C.J., Spearing, M.C., 1995. Void space modeling of mercury intrusion hysteresis in sandstone, paper coating and other porous media. J. Colloid Interface Sci. 171, 8.
Murray, K.L., Seaton, N.A., Day, M.A., 1999. An adsorption-based method for the characterization of pore networks containing both mesopores and macropores. Langmuir 15, 6728–6737.
Nepryahin, A., Fletcher, R.S., Holt, E.M., Rigby, S.P., 2016. Structure-transport relationships in disordered solids using integrated rate of gas sorption and mercury porosimetry. Chem. Eng. Sci. 152, 663–673.
Petrobank, 2008. Whitesands experimental project IETP annual report. http://www.energy.alberta.ca/3040.asp, Accessed date: 20 October 2017.
Petrobank, 2010. Whitesands experimental project IETP annual report. http://www.energy.alberta.ca/3261.asp, Accessed date: 20 October 2017.
Pooladi-Darvish, M., Mattar, L., 2002. SAGD operations in the presence of overlying gas cap and water layer-effect of shale layers. J. Can. Pet. Technol. 41.
Rabiu Ado, M., 2017. Numerical Simulation of Heavy Oil and Bitumen Recovery and Upgrading Techniques. PhD thesis. University of Nottingham. http://eprints.nottingham.ac.uk/41502/.
Rabiu Ado, M., Greaves, M., Rigby, S., 2019. Numerical simulation of the impact of geological heterogeneity on performance and safety of THAI heavy oil production process. J. Pet. Sci. Eng. 173, 1130–1148. https://doi.org/10.1016/j.petrol.2018.10.087.
Rigby, S.P., 2018. Recent developments in the structural characterisation of disordered, mesoporous solids. Johnson Matthey Technol. Rev. 62 (3), 296–312.
Tsakiroglou, C.D., Payatakes, A.C., 1991. Effects of pore-size correlations on mercury porosimetry curves. J. Colloid Interface Sci. 146, 479.
Uguna, C.N., Carr, A.D., Snape, C.E., Meredith, W., Castro-Díaz, M., 2012. A laboratory pyrolysis study to investigate the effect of water pressure on hydrocarbon generation and maturation of coals in geological basins. Org. Geochem. 52, 103–113.
Uguna, C.N., Carr, A.D., Snape, C.E., Meredith, W., 2015. High pressure water pyrolysis of coal to evaluate the role of pressure on hydrocarbon generation and source rock maturation at high maturities under geological conditions. Org. Geochem. 78, 44–51.
Uguna, C.N., Carr, A.D., Snape, C.E., Meredith, W., Scotchman, I.C., Murray, A., Vane, C.H., 2016. Impact of high water pressure on oil generation and maturation in Kimmeridge Clay and Monterey source rocks: implication for petroleum retention and gas generation in shale gas systems. Mar. Pet. Geol. 73, 72–85.
Walker, W.C., Zettlemoyer, A.C., 1948. A dual-surface BET adsorption theory. J.Phys. Colloid Chem. 52, 47–58.
Wardlaw, N.C., McKellar, M., 1981. Mercury porosimetry and the interpretation of pore geometry in sedimentary rocks and artificial models. Powder Technol. 29, 127–143.
Whitelaw, P., Uguna, C.N., Stevens, L.A., Meredith, W., Snape, C.E., Vane, C.H., Moss-Hayes, V., Carr, A., 2019. Shale gas reserve evaluation by laboratory pyrolysis and gas holding capacity consistent with field data. Nat. Commun (in press).